Available online at www.sciencedirect.com

ScienceDirect

Advances in Space Research 64 (2019) 527–544

ADVANCES IN SPACE RESEARCH (a COSPAR publication)

www.elsevier.com/locate/asr

Seismology on small planetary bodies by orbital laser Doppler vibrometry

Paul Sava [a,*], Erik Asphaug [b]

[a] Center for Wave Phenomena, Colorado School of Mines, 1500 Illinois Street, Golden, CO 80401, USA
[b] Lunar and Planetary Laboratory, University of Arizona, 1629 E University Blvd, Tucson, AZ 85721, USA

Received 20 October 2018; received in revised form 23 March 2019; accepted 15 April 2019
Available online 24 April 2019

Abstract

The interior structure of small planetary bodies holds clues about their origin and evolution, from which we can derive an understanding of the solar system's formation. High resolution geophysical imaging of small bodies can use either radar waves for dielectric properties, or seismic waves for elastic properties. Radar investigation is efficiently done from orbiters, but conventional seismic investigation requires landed instruments (seismometers, geophones) mechanically coupled to the body.

We propose an alternative form of seismic investigation for small bodies using Laser Doppler Vibrometers (LDV). LDVs can sense motion at a distance, without contact with the ground, using coherent laser beams reflected off the body. LDVs can be mounted on orbiters, transforming seismology into a remote sensing investigation, comparable to making visual, thermal or electromagnetic observations from space. Orbital seismometers are advantageous over landed seismometers because they do not require expensive and complex landing operations, do not require mechanical coupling with the ground, are mobile and can provide global coverage, operate from stable and robust orbital platforms that can be made absolutely quiet from vibrations, and do not have sensitive mechanical components.

Dense global coverage enables wavefield imaging of small body interiors using high resolution terrestrial exploration seismology techniques. *Migration* identifies and positions the interior reflectors by time reversal. *Tomography* constrains the elastic properties in-between the interfaces. These techniques benefit from dense data acquired by LDV systems at the surface, and from knowledge of small body shapes. In both cases, a complex body shape, such as a comet or asteroid, contributes to increased wave-path diversity in its interior, and leads to high (sub-wavelength) imaging resolution.
© 2019 COSPAR. Published by Elsevier Ltd. All rights reserved.

Keywords: Comet; Asteroid; Laser; Vibrometer; Seismic; Imaging; Tomography

1. Introduction

Asteroids and comets stimulate increased interest with every mission of discovery, Fig. 1. Answering questions about their origin and evolution (Asphaug, 2009) comes down to an understanding of their internal structure, the one aspect we cannot measure, to date, from any remote sensing platform, or by any current-capability landed science platform. The internal structure is often inferred from surface observations, for instance that asteroid Itokawa is a rubble pile (Fujiwara et al., 2006) or that comet 67P/Churyumov-Gerasimenko (67P/C-G) is a weak, layered primordial agglomeration (Massironi et al., 2015). General aspects of the interior are made available from radar measurements (Ciarletti et al., 2017), for instance that the interior of comet 67P/C-G appears homogeneous along the integrated radar paths. These inferences in turn lead to ideas about how the solar system and the planets

* Corresponding author.
E-mail address: psava@mines.edu (P. Sava).

https://doi.org/10.1016/j.asr.2019.04.017
0273-1177/© 2019 COSPAR. Published by Elsevier Ltd. All rights reserved.

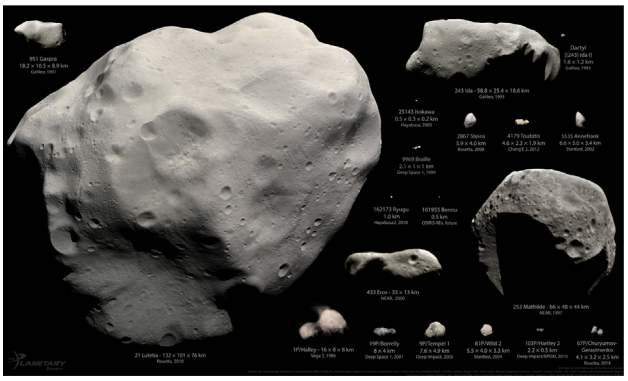


Fig. 1. Comets and asteroids visited by spacecraft and characterized by different irregular shapes and sizes. (Credits: Emily Lakdawalla, planetary.org).

came together, e.g. quiescently or violently, and how small bodies such as near-Earth asteroids respond to collisions.

Consider Phobos, orbiting Mars. Is it indeed a powdery rubble pile as some recent models (Hurford et al., 2016) and origin theories suggest, or is it a rigid fractured monolith? A seismic image of its interior would reveal past history of fragmentation, disruption and reaccretion, and would extend surface fissures, if that is what they are, to structures throughout the deep interior, indicating the nature of its tidal response to Mars. Consider cometary nuclei, emissaries from the distant reaches of the solar system. Are they fragments of parent bodies, as dynamical models would imply? Or are they primitive accretionary bodies, the popular but far from unanimous view after the Rosetta mission?

Another motivation for imaging the interior structure of small bodies is pragmatic, i.e. the need to deflect or destroy hazardous near-Earth objects (NEOs). It is clear, from detailed collisional modeling (Bruck Syal et al., 2016I) that the response of a targeted asteroid to a kinetic missile or explosion is sensitive to its internal structure. A mechanically disconnected object, e.g. a rubble pile or contact binary, responds very differently from a cohesive body, and a weak interior limits the amount of deflection momentum that can be applied without disrupting it into fragments that could individually threaten Earth. Unfortunately it is generally unknowable, with decades of warning, whether a given asteroid will definitely strike Earth. Objects like 99942 Apophis travel through Earth's dynamical space and may or may not impact at some time in the future. Asteroids that rank relatively high on the Torino or Palermo scales (Morrison et al., 2004; Binzel et al., 2015) merit detailed geophysical investigation, but such investigations are costly. It is necessary to develop **low-cost missions** that can interrogate internal structure **without landed operations**.

Various methodologies have been considered to answer the open question of 3D internal structure of small bodies. One is radar imaging, for example using wavefield techniques (Sava et al., 2015; Sava and Asphaug, 2018a,b), which can in principle image internal structures by mapping dielectric contrasts and reflectors. In practice this technique says little about internal mechanical properties, for instance whether a feature is a plane of weakness or just a compositional boundary. From the point of hazard mitigation, the key question of interest is how the body responds to stress waves, not electromagnetic waves. Like radar, seismology also maps internal contrasts and reflectors, but using elastic wave propagation through solid and granular media. This in turn leads to maps of internal structure, as well as to characterization of strength and bulk granular properties of asteroid materials.

As exploration of the solar system continues, the drive to attempt seismology on remote small planetary bodies becomes more prominent. Historically, landed systems have been considered necessary for doing seismology, which leads to small body missions of high cost and complexity. A landed network of seismic stations is prohibitively expensive given the requirement to assess an increasing number of potentially hazardous asteroids, as well as the desire to survey resource-rich prospects, and to conduct reconnaissance of targets for human voyages and other asteroid missions. Thomas and Robinson (2005) attribute the regional denudation of 100 m craters on the $\sim 33 \times 13 \times 13$ km asteroid 433 Eros to seismic resurfacing by the last large cratering event. They were thus able to conduct seismology of a speculative sort, by counting craters. Eros, they concluded, had to be seismically transmissive, and relatively homogeneous at 100 m scales, in order for its largest recent crater to have shaken down prior 100 m craters. A more general study (Asphaug, 2008) shows that the largest un-degraded crater on an asteroid can be a quantitative indicator of seismic attenuation in asteroid material. The problem of imaging complex asteroid interiors was also studied by Richardson et al. (2005) and Blitz (2009). Nevertheless, no seismic mission to a small body has been conducted to-date, primarily due their implied high cost and complexity.

In this paper, we advocate for a low-cost approach to **3D seismic imaging** on comets and asteroids from a **remote sensing platform,** using an instrument that can be carried on small spacecraft to dozens of NEOs, as well as to moons, comets and other small bodies. While science requirements may vary depending on the specific question and the nature of the target (e.g. layering and activity in cometary nuclei, or subsurface expressions of groove structures on Phobos, or mean block size on a small NEO), we set the general objective to recover the internal structure of a 0.3–30 km diameter small body of arbitrary shape at a resolution comparable to the seismic wavelength. As we show in the following sections, this requirement is met using reflection seismology with data acquired by laser Doppler vibrometry from an orbiter and exploiting full wavefield data processing.

2. Extraterrestrial seismology

Seismology on other worlds started with seismic experiments performed during the manned Apollo missions to the Moon from 1969 to 1977 (Tong and Garcia, 2015). The Apollo experiments used both passive (e.g. meteorite impacts, tidal forces) and active sources (e.g. explosions, spacecraft crashes). A small number of seismometers and geophones were deployed during several Apollo missions and lead to an understanding of the Moon interior structure, of the spatial and temporal distribution of moonquakes, and of physical parameters characterizing Moon rocks. Mars seismology was attempted by Viking missions from 1976 to 1978, without much success since the seismometers were not deployed to the surface, but remained mounted on the lander where they did not record any seismic activity. No other seismic instrument was active on any planetary body until the InSight mission brought its seismometer to Mars in 2018. The single InSight seismometer will give important information about the general internal structure of Mars, but cannot be used for 3D high resolution seismic imaging because it does not provide multiple views in the interior of the planet.

Seismology on small bodies (comets, asteroids, small moons) has not been attempted to date, primarily due to the difficulty and risk of deploying suitable landers. Seismometer coupling to the surface in microgravity environments is extremely difficult, both because anchoring technology is immature and because the surface materials are not sufficiently understood to determine how effectively they can transfer ground vibrations. Moreover, conventional Earth seismometers with suspended masses are ineffective in micro-gravity environments (Tong and Garcia, 2015), and reducing environmental noise requires their deployment inside complex vacuum-sealed enclosures, as is the case for the InSight instrument on Mars (Banerdt et al., 2013). Nevertheless, because of the high science impact, several seismic payloads have been proposed for the Moon, e.g. JAXA/SELENE2 (Tanaka et al., 2013) and NASA/Lunette (Neal et al., 2011), and for Mars, e.g. ESA/Inspire (Voirin et al., 2014), and for Europa (Gowen et al., 2011).

A seismic system consists of *sources*, which can be either natural or artificial, and *receivers*. In this paper, we focus on the receivers which could be of two main categories, landed and orbital, as discussed next.

2.1. Landed seismology

A good understanding of the interior structure of a small planetary body requires observations from multiple directions, analogous to the methods used to form medical images (tomograms) with instruments deployed around the studied body. Terrestrial 3D seismic imaging technology is well-developed, e.g. in seismic exploration (Sherriff and Geldart, 2010) or in global seismology (Nolet, 2008), and it takes advantage of two main opportunities:

- instruments are tightly coupled to the ground, and
- seismometers form dense distributed networks (antennas).

Neither condition can be satisfied with conventional instruments (seismometers or geophones) on a small body. All mission concepts that emplace seismometers on the surface of a small planetary body, e.g. BASiX (Scheeres et al., 2014), face many complex challenges. Anchoring a seismology package to a small body requires robust technology that does not yet exist. A small lander deployed from an orbiter would be at rest on the surface materials, which themselves may be loosely consolidated, and so the seismic signals would be difficult to interpret. In addition, the complexity of a landed package with seismology instrumentation raises the cost of a mission and increases its risk. Finally, strong seismic waves caused, e.g., by an impact or an explosion, could dislodge the payload from the surface, which would then remain lofted in microgravity and possibly bounce off the surface instead of recording seismic data. Together these challenges have led to consideration of increasingly complex methods for embedding geophone or seismometer payloads into a comet or asteroid subsurface, where thermal, power, mechanical and communications issues become substantial. Given this cost and complexity, a dense distributed network of landed seismometers is out of question for a realistic mission to a small body.

2.2. Orbital seismology

The main purpose of ground coupling is to capture its vibration with an instrument that converts ground motion into an electrical signal. We seek to remove this basic constraint and thus eliminate the need for instrument surface deployment altogether.

Our solution uses laser Doppler vibrometry which is described in detail in the following section. A Laser Doppler Vibrometer operates by sending a laser beam to a moving target (e.g. the ground surface), and then observing the Doppler frequency shift of the reflected laser beam caused by ground motion. LDVs used as seismometers have numerous technical advantages over conventional landed seismometers:

1. take measurements from orbit, thus avoiding expensive landers;
2. do not use mechanical ground coupling, thus avoiding anchors;
3. have simple electronic design, without fragile mechanical components;

4. are mobile and can measure ground motion at distributed locations;
5. utilize stable orbital platforms that are decoupled from ground noise.

Non-contact seismology using LDVs reduces dramatically the acquisition cost by avoiding landing, and increases significantly spatial coverage by using mobile and long-lived instruments. These benefits simplify the design and execution of a remote seismology mission, while providing data with wide spatial coverage capable to image in detail the 3D internal structure of complex small planetary bodies.

Laser sensing technology is not new in space environments. Laser altimetry is routinely used in space applications and can operate successfully at distances as large as 50 km (Smith et al., 2010; Zuber et al., 2010). Laser Doppler vibrometers share many of the optical technology used by laser altimeters, but use continuous, instead of pulsed lasers. Orbital LDVs have several significant advantages over their terrestrial counterparts, which can greatly increase their sensing distance.

- First, the orbital laser sensor is mounted on a stable platform in vacuum, which does not add measurement noise as long as no attitude control (ACS) or navigation maneuvers occur during sensing. In contrast, terrestrial LDVs are subject to undesirable vibrations caused by environmental factors (e.g. wind or human activity).
- Second, the laser beam of an orbital LDV propagates through vacuum, and thus it is not subject to scattering caused by air and suspended particles in-between the laser head and the reflecting surface, as is the case for terrestrial systems.

These features enable LDVs to operate at larger distances than what would be possible in terrestrial environments.

Laser Doppler vibrometers are used extensively in industrial settings, primarily to sense motion of small mechanical components (e.g. MEMS), distant objects (e.g. bridges) or hazardous targets (e.g. turbines). Common long range terrestrial LDV can measure vibrations at hundreds of meters with instruments comparable in size with a 6U cubesat. Terrestrial LDVs are designed specifically for distances smaller than a few hundred meters and operate with low laser power in order to ensure eye safety in open environments and portability with small telescopes (diameter < 10 cm). Various elements of an LDV system scale-up for larger sensing distances, i.e. space applications can use more powerful lasers because eye safety is not a concern, and can also use larger telescopes tuned to the expected distance of investigation. Nevertheless, the general design of an LDV system remains the same regardless of sensing distance, as discussed in the following section.

We concentrate on the key aspects of seismology using orbital laser Doppler vibrometry, including the concepts of operation and the wavefield imaging framework, and leave a complete discussion of instrument sensitivity and intrinsic noise outside the scope of this paper.

3. 1D laser Doppler vibrometry

Laser vibrometers exploit the Doppler principle (Appendix A), and are constructed with optical components as sketched in Fig. 2, (Donges and Noll, 2015). An important characteristic of LDVs is that they do not rely on mechanical components whose performance might degrade over time in space environments. Instead, LDVs are based on optical components which have a long and successful track record in space missions.

Laser Doppler vibrometers function as follows, Fig. 2: A laser beam of known wavelength is split at the beam splitter BS1 into a *reference beam* (blue line) and an *incident beam* (red line). The incident beam is focused using a telescope on a distant vibrating object, for example the surface of a small body. The *reflected beam* (green line), is characterized by a different frequency as a result of the Doppler effect caused on the laser beam by the motion of the ground. As discussed later, the frequency shift is proportional with the velocity of the ground in the direction of the laser beam. The reflected beam is captured through the same or a different telescope, and it is guided through beam splitter BS2 to the detector. Similarly, the reference beam is guided to the detector using beam splitter BS3. The reference and reflected laser beams are combined to form a composite signal with frequency modulated by the mismatch between their frequencies.

To further illustrate the functionality of an LDV, let's consider reference and reflected beams represented by harmonic waves with amplitudes A_i and A_r, frequencies f_i and f_r, and phases ϕ_i and ϕ_r, respectively:

$$\begin{cases} E_i = A_i e^{i(2\pi f_i t + \phi_i)}, \\ E_r = A_r e^{i(2\pi f_r t + \phi_r)}. \end{cases} \tag{1}$$

The reference and reflected beams sum at the detector, Fig. 3,

$$E = E_i + E_r, \tag{2}$$

and therefore the total detected light intensity is

$$I \equiv EE^* = E_i E_i^* + 2E_i E_r + E_r E_r^* \tag{3}$$

$$= I_i + 2\sqrt{I_i I_r} cos[2\pi(f_r - f_i)t + (\phi_r - \phi_i)] + I_r, \tag{4}$$

where the symbol * indicates complex conjugate, and $I_i = A_i^2$ and $I_r = A_r^2$ are the intensities of the incident and the reflected beams, respectively. Using the Doppler shift $f_r - f_i = \frac{2}{\lambda_i} v$ (Appendix A), we obtain

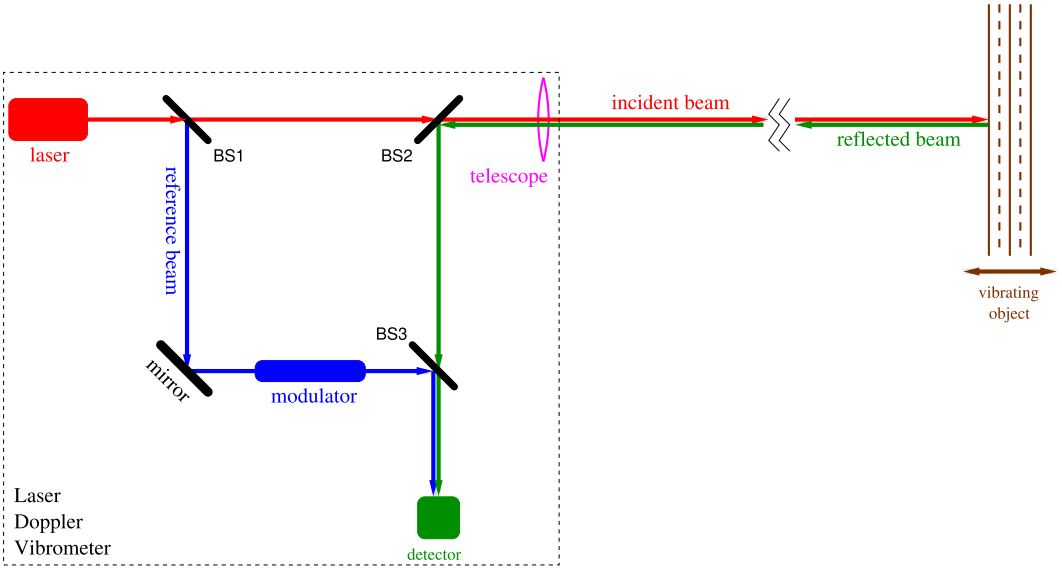


Fig. 2. Key components of a laser Doppler vibrometer system: laser (red), modulator (blue), detector (green), telescope (magenta), beam splitters and mirrors (black). (For interpretation of the references to colour in this figure legend, the reader is referred to the web version of this article.)

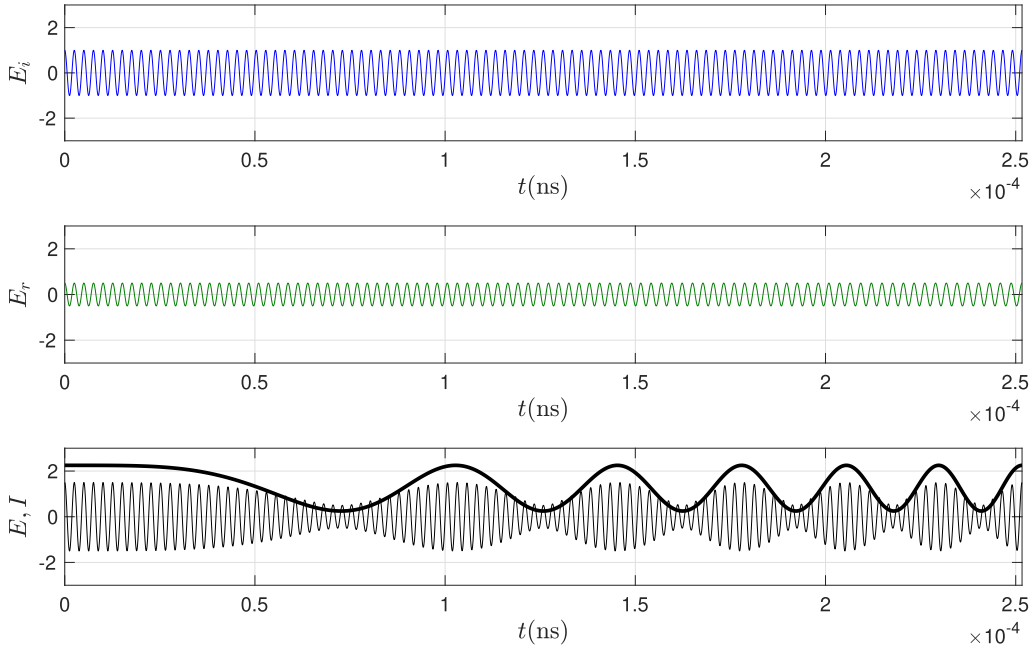


Fig. 3. Simulation of the incident laser beam (top panel), the reflected laser beam (middle panel) and the superposition of the two laser beams (bottom panel, thin line). The total intensity I at the detector (bottom panel, thick line) is characterized by the beat frequency f_b which is related to the ground velocity.

$$I = I_i + 2\sqrt{I_i I_r}cos\left[2\pi\left(\frac{2}{\lambda_i}v\right)t + (\phi_r - \phi_i)\right] + I_r. \quad (5)$$

The total laser intensity at the detector is an oscillatory function whose frequency, known as the *beat frequency*, is

$$f_b = \frac{2}{\lambda_i}|v|. \quad (6)$$

The beat frequency can be observed (demodulated) from the combined intensity signal, thus providing a measurement of the ground velocity in the direction of the laser beam.

The total intensity function also depends on the amplitudes of the incident and reflected laser beams. The incident beam is known by design and depends on the laser parameters. The reflected beam, however, depends also on the reflectivity (albedo) of the small body surface. This parameter varies greatly and depends both on the physical properties of the small body surface, but also on the wavelength of the laser. The albedo of small planetary bodies is

usually dark (Nesvorný et al., 2015), with values ranging from 3% to 30% depending on the material type. For low albedo values, the intensity of the reflected laser beam is proportionally small. Nevertheless, an appropriately constructed LDV with wide telescope aperture (tens of cm) and sensitive light sensors can operate well at distances of km for surfaces with albedo ~4%. The reflected light intensity is only needed to ensure appropriate signal-to-noise ratio at the detector, and is not a direct factor for velocity measurement which is controlled by the beat frequency of the combined intensity signal, Fig. 3.

The key insight provided by Eq. (6) is that the beat frequency depends on the known laser wavelength λ_i and the component of the ground velocity oriented in the direction of the incident laser beam. Therefore, measuring the beat frequency f_b, we can calculate the ground velocity v. However, Eq. (6) shows that the beat frequency depends on the absolute value of the ground velocity, and thus it cannot be used directly to also evaluate the direction of ground motion.

A well-established solution to this problem is to create a large artificial frequency shift of the reference beam prior to combining it with the reflected beam. This can be achieved using an acousto-optic modulator, also known as a Bragg cell (Donges and Noll, 2015), Fig. 2. If the reference beam is shifted by frequency f_o, then the total laser intensity observed at the detector is

$$I = I_i + 2\sqrt{I_i I_r}cos\left[2\pi\left(\frac{2}{\lambda_i}v + f_o\right)t + (\phi_r - \phi_i)\right] + I_r, \quad (7)$$

where f_o is the Bragg frequency. Consequently, the beat frequency is

$$f_b = \frac{2}{\lambda_i}\left|v + \frac{\lambda_i}{2}f_o\right|, \quad (8)$$

which reduces to Eq. (6) for $f_o = 0$ Hz. Fig. 4 is a graphical illustration of Eq. (8) showing that beat frequencies lower and higher than f_o correspond to negative and positive velocities, respectively. Conventionally, it is assumed that velocities are greater than $-\frac{\lambda_i}{2}f_o$ and lower than $+\frac{\lambda_i}{2}f_o$, although the upper bound is not actually needed.

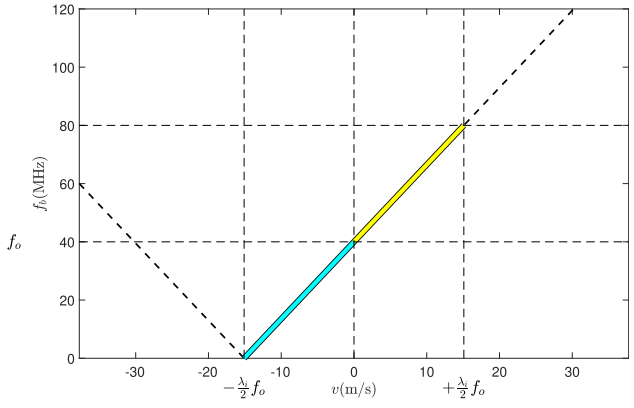


Fig. 4. Representation of the frequency (black) as a function of ground velocity for a laser with wavelength $\lambda = 755$ nm, assuming a Bragg shift $f_o = 40$ MHz. Beat frequencies lower than f_o correspond to negative velocities (cyan), while beat frequencies higher than f_o correspond to positive velocities (yellow), according to Eq. (8). (For interpretation of the references to colour in this figure legend, the reader is referred to the web version of this article.)

Long range LDVs are designed to operate in daylight which is much brighter than the laser light. However, LDVs function appropriately even in these conditions because the laser has a precise and known wavelength, while the ambient light scatters uniformly at all wavelengths. The interference between the two is minimal, thus allowing LDVs to function in both daytime and nighttime, albeit at a slightly lower SNR in daytime conditions.

Laser scattering off natural (irregular) surfaces is subject to so-called speckle noise, caused by interference between light originating at randomly distributed scatterers. This is a known phenomenon in laser Doppler vibrometry (Guo et al., 2001; Drabenstedt, 2007). Strategies to mitigate this phenomenon include combination of data acquired by multiple co-located detectors, similarly to the methodology used by orbital LIDAR systems (Smith et al., 2010; Zuber et al., 2010). We leave a complete treatment of this and other noise sources and mitigation strategies outside the scope of this paper.

4. 3D laser Doppler vibrometry

Conventional LDV acquisition recovers the ground velocity in the direction of the laser beam. Formally, the LDV measurement represents the projection of the ground velocity vector onto the vector defining the direction of the laser beam. However, vector acquisition is also possible if three or more LDVs separated in space, for example on small satellites or cubesats, observe ground motion at the same location, Fig. 6(a)–(c).

3D laser Doppler vibrometry exploits the property that laser beams reflect off small body surfaces at broad angles. We can assume that small bodies are described by Lambertian, or perfectly diffuse, surfaces (Lucey et al., 2014; Daly et al., Oct 2017), as is the case for many natural surfaces. Under this assumption, the intensity of light reflected off a surface does not depend on the reflection direction. However, the reflected light intensity depends on the incident light intensity projected on the normal to the surface (known as the Lambertian cosine law). Fig. 5 illustrates this idea: the black and red vectors represent the normal to the Lambertian surface and the direction of an incoming laser beam at an angle relative to the normal, as marked on the figure. The reflection intensity depends on the dot product between the two vectors, i.e. follows the cosine law, and is the same in all directions, as indicated by the spherical domes.

The practical consequence of interacting with Lambertian ground surfaces is that a laser beam reflects back to the LDV regardless of angle of incidence on the small body surface. The preferred direction of LDV investigation is close to the ground surface normal, but vibrometry can

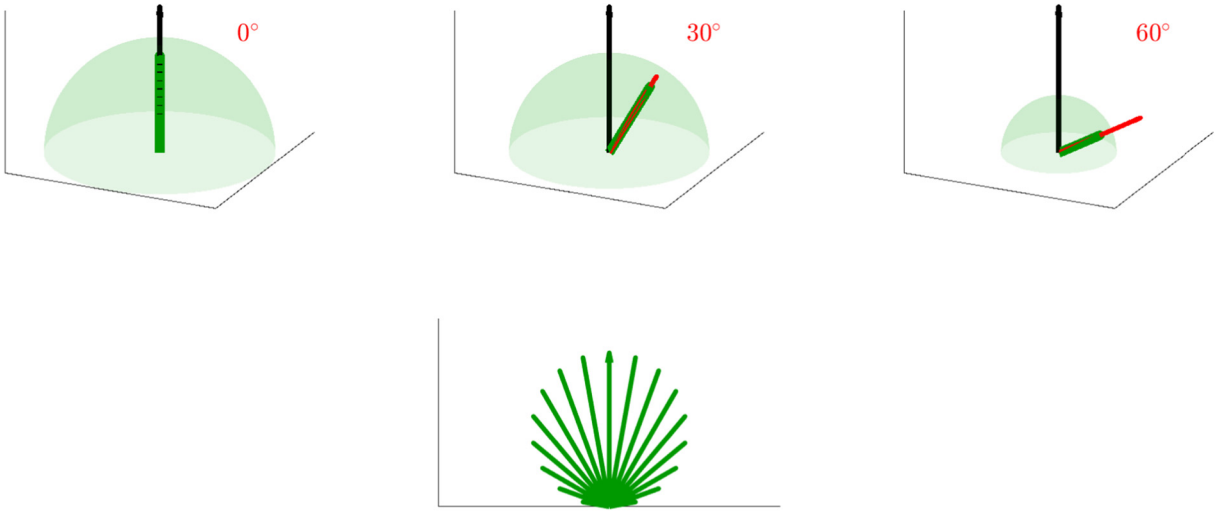


Fig. 5. Illustration of laser reflection off a Lambertian surface. The reflected light intensity, i.e. the radii of the spherical domes, depends on the angle of incidence (top panels), and follows the cosine law (bottom panel).

be conducted effectively at other angles. As the angle between the laser beam and the normal increases, the amount of reflected light decreases according to the cosine law. This reduction in laser light intensity would not be a problem for an LDV sized appropriately to function with reduced light intensity (i.e. an LDV with a larger receiver telescope and sensitive light sensors).

Therefore, we can consider an acquisition scenario in which the ground velocity at a point is observed with multiple orbiting LDVs, e.g. three, at different (possibly large) angles relative to the surface normal. With such coordinated LDV observations, we could collect all the information necessary to reconstruct the ground velocity vector.

If we consider three orbiting LDVs and denote the vectors connecting a given ground observation point to the three LDVs by

$$\mathbf{a} = [a_x\ a_y\ a_z]', \tag{9}$$

$$\mathbf{b} = [b_x\ b_y\ b_z]', \tag{10}$$

$$\mathbf{c} = [c_x\ c_y\ c_z]', \tag{11}$$

then we can represent the projection of the ground velocity vector

$$\mathbf{v} = [v_x\ v_y\ v_z]' \tag{12}$$

by

$$\mathbf{p} = [p_a\ p_b\ p_c]'. \tag{13}$$

The formal relation between $\mathbf{v}$ and $\mathbf{p}$ (Miyashita and Fujino, 2006; Rothberg et al., 2017) is

$$\mathbf{p} = \mathbf{P}\mathbf{v}, \tag{14}$$

where $\mathbf{P}$ is a projection matrix defined using the components of the LDV position vectors $\mathbf{a}$, $\mathbf{b}$ and $\mathbf{c}$:

$$\mathbf{P} = \begin{bmatrix} a_x & a_y & a_z \\ b_x & b_y & b_z \\ c_x & c_y & c_z \end{bmatrix}. \tag{15}$$

Eq. (14) can in principle be used to determine the ground velocity vector $\mathbf{v}$ from the projection vector $\mathbf{p}$. However, this requires that the vectors $\mathbf{a}$, $\mathbf{b}$ and $\mathbf{c}$ are significantly different from one-another to ensure that the projection matrix Eq. (15) is non-singular, or more precisely that the projection matrix has a low condition number. Otherwise, the velocity reconstruction amplifies the noise present in the LDV data. Fig. 6(d) and (e) illustrate this idea with a simulation of ground motion as a chirp with frequency linearly increasing from 0.1 to 10 Hz, with 5% random noise. At 10° aperture, the ground velocity reconstruction is significantly noisier than at 30°, as visualized by the corresponding spectral density curves, Fig. 6(g) and (h). We note that the noise used in this simulation is for illustration purposes, and does not reflect the expected LDV instrument or observation noise.

We can improve the ground velocity vector reconstruction if we recast it as an inverse problem and use data coherency over time for regularization. Using this formulation, we seek to reconstruct the vector

$$\mathbf{m} = \begin{bmatrix} \mathbf{v}_1 \\ \mathbf{v}_2 \\ \vdots \end{bmatrix} \tag{16}$$

where $\mathbf{v}_i$ represent the ground motion at different times indexed by i. We determine $\mathbf{m}$ using the data vector

$$\mathbf{d} = \begin{bmatrix} \mathbf{p}_1 \\ \mathbf{p}_2 \\ \vdots \end{bmatrix} \tag{17}$$

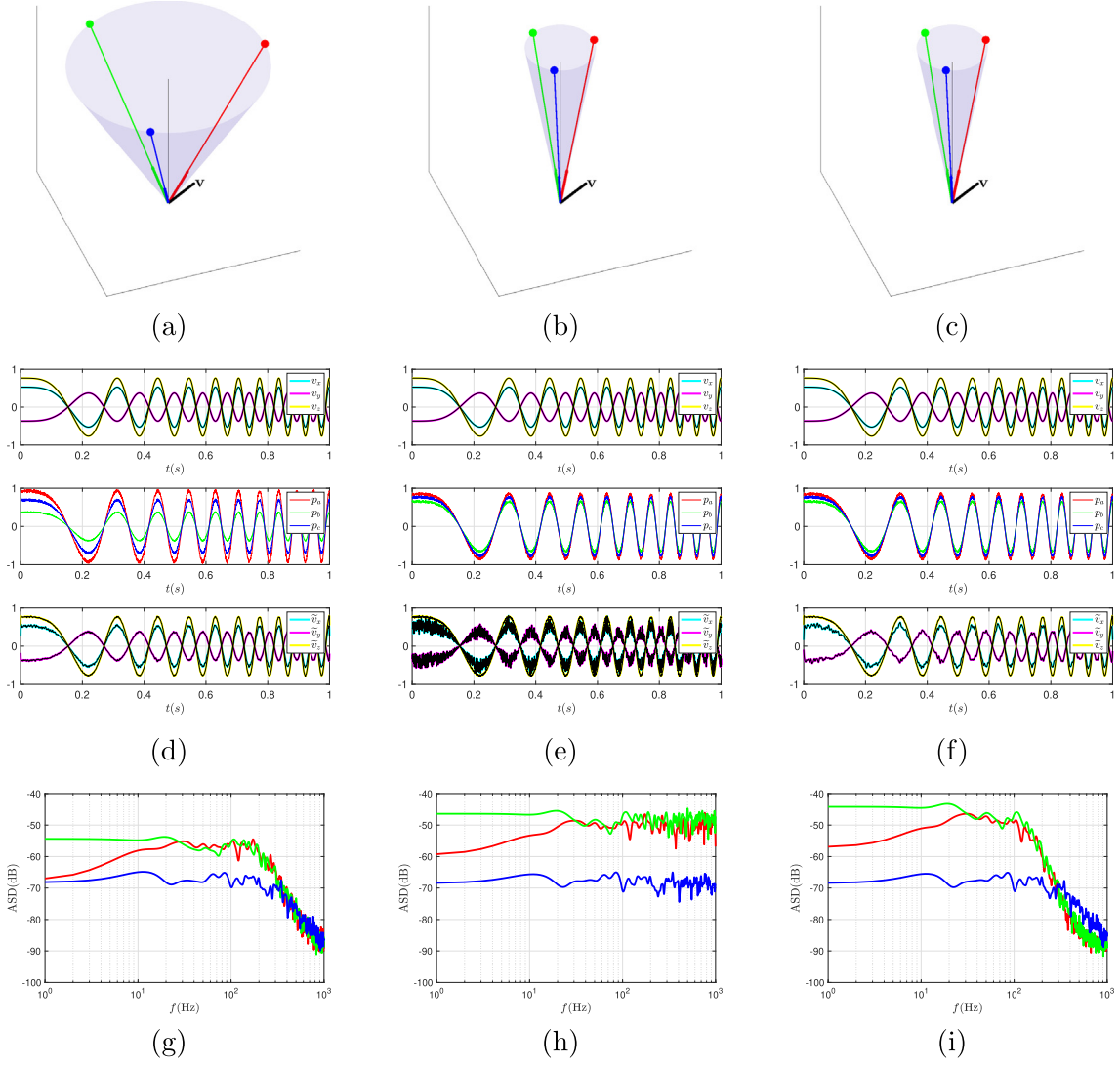


Fig. 6. Illustration of vector ground velocity acquired using 3 orbiters (red, green, blue) for (a) 30° and (b), (c) 10° aperture. Panels (d), (e) and (f) are time series representing from top to bottom, the (normalized) ground velocity vector $\mathbf{v}$, the vector projections on the laser beams from three LDVs $\mathbf{p}$, and the vector reconstruction $\tilde{\mathbf{v}}$. Panels (g), (h) and (i) show the spectral density of the noise contaminating the time series in panels (d), (e) and (f), respectively. (For interpretation of the references to colour in this figure legend, the reader is referred to the web version of this article.)

where $\mathbf{p}_i$ represents the ground velocity projections at times similarly indexed by i. With this notation, we can reformulate the reconstruction problem as follows: find $\mathbf{m}$ to minimize an objective function J

$$\min_{\mathbf{m}} 2J = \|\mathbf{Gm} - \mathbf{d}\|^2 + \epsilon^2 \|\mathbf{Rm}\|^2, \tag{18}$$

where $\mathbf{G}$ is a projection operator defined for all times

$$\mathbf{G} = \begin{bmatrix} \mathbf{P} & 0 & \dots \\ 0 & \mathbf{P} & \dots \\ \vdots & \vdots & \ddots \end{bmatrix}, \tag{19}$$

and $\mathbf{R}$ is a regularization operator (a second derivative, for example), seeking to reconstruct the smoothest model $\mathbf{m}$:

$$\mathbf{R} = \begin{bmatrix} -2\mathbf{I} & \mathbf{I} & \dots \\ \mathbf{I} & -2\mathbf{I} & \dots \\ \vdots & \vdots & \ddots \end{bmatrix}. \tag{20}$$

The scalar parameter ϵ balances data fitting with model shaping, i.e. the relative importance between the terms of Eq. (18). In practice, this parameters can be obtained through direct data analysis, using e.g. the L-curve approach (Aster et al., 2005). With this notation, the denoised ground motion vectors at all times are obtained by

$$\tilde{\mathbf{m}} = \left(\mathbf{G}^\top \mathbf{G} + \epsilon^2 \mathbf{R}^\top \mathbf{R}\right)^{-1} \mathbf{G}^\top \mathbf{d} \tag{21}$$

Fig. 6(f)–(i) illustrate this method with the simulation shown in Fig. 6. At 10° aperture, the regularized ground velocity is significantly less noisy than the conventional (un-regularized) reconstruction, Fig. 6(e)–(h).

5. Small body seismicity

Small body seismic investigation depends on a few key parameters that define their seismicity. In particular, the LDV response depends on the ground velocity in the direction of the incident laser beam. Ground velocity in turn depends on the magnitude of the ground displacement, as well as the seismic wave frequency. Using ground velocity, we can account for the Doppler shift which is related to the beat frequency, as discussed in the preceding sections.

Consider a monochromatic wave of frequency f causing ground displacement of magnitude u:

$$u_p = u \sin(2\pi f t). \tag{22}$$

The velocity of a particle on the ground is

$$v_p = v \cos(2\pi f t), \tag{23}$$

with velocity magnitude

$$v = 2\pi f u. \tag{24}$$

Then, the maximum observable Doppler frequency shift is

$$\Delta f = \frac{2}{\lambda_i} v, \tag{25}$$

which is directly proportional with the magnitude of the velocity vector, Eq. (24). In order to evaluate ground velocities and associated Doppler frequency shifts, we consider a range of possible frequencies f and ground displacements u likely to occur on a small body.

Fig. 7(a)–(c) show comet and asteroid shapes in the range of body sizes we consider in this paper. For the type

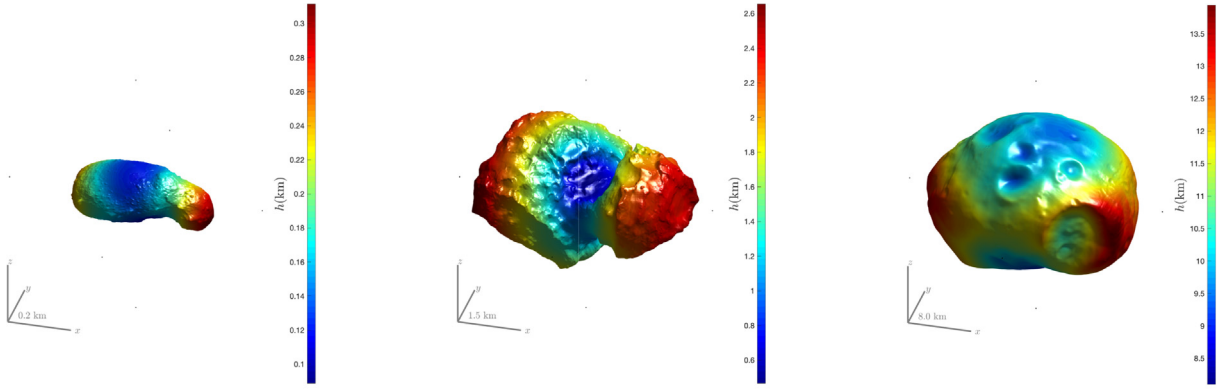


Fig. 7. Models of small planetary bodies of different sizes and shapes. Approximate diameters range from 0.3 to 30 km. The colors depict distance from the body center of mass. The shape models represent asteroid 25143 Itokawa, comet 67P/C-G and Mars' moon Phobos. (For interpretation of the references to colour in this figure legend, the reader is referred to the web version of this article.)

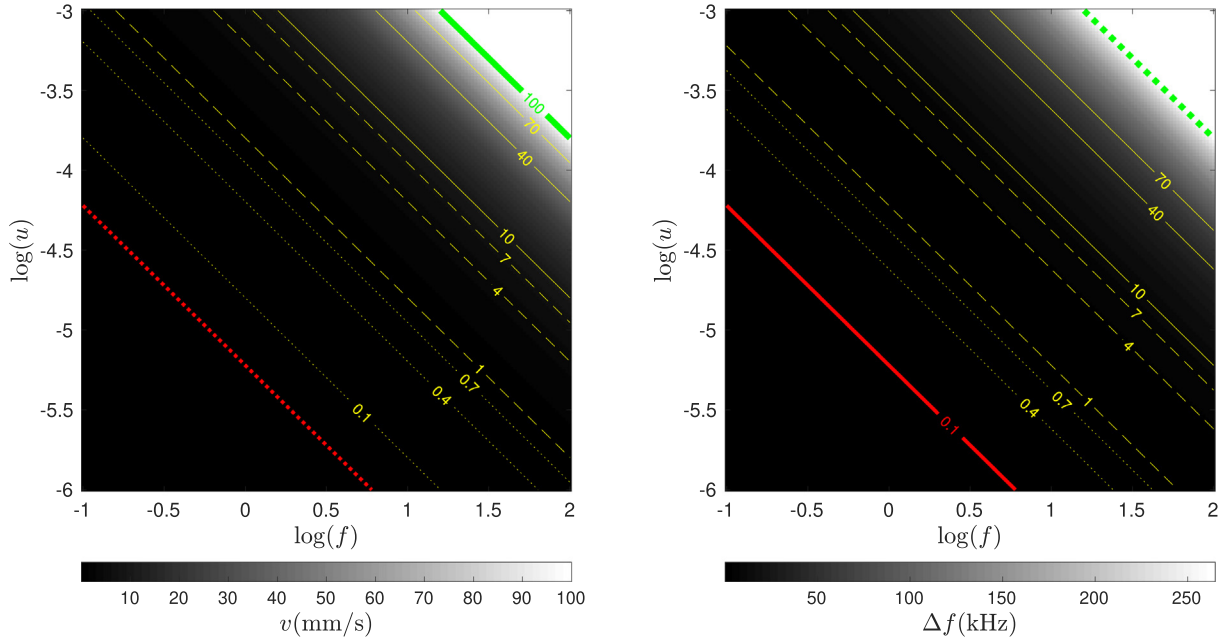


Fig. 8. Representation of ground velocity (left) and Doppler frequency shift (right) as a function of seismic frequency and ground displacement.

of interior imaging discussed later, we seek to distinguish features that are much smaller than the representative dimension of the body. We assume that the peak seismic frequency is large enough such that a significant number of wavelengths, e.g. 10, fit within the mean body diameter. For example the bodies depicted in Fig. 7(a)–(c) have approximate diameters between 0.3 and 30 km, and therefore need to be investigated with representative wavelengths between 0.03 and 3 km. Assuming propagation velocities between 0.3 and 3 km/s, we obtain frequencies between 0.1 and 100 Hz. Likewise, if we assume relatively weak interior seismic sources, we could observe ground displacements between 1 μm–1 mm.

Fig. 8 summarizes the distribution of peak velocities and associated Doppler shifts as a function of frequencies and displacements. Some ground velocities are too large to be feasible on a low-gravity small body. For example, if we assume an escape velocity of 1 m/s, appropriate for an object of the size and mass of comet 67P/C-G, then we can set the range of possible ground velocities that would allow surface particles to remain attached to the ground to, e.g., 10% of the escape velocity. In Fig. 8, all ground velocities greater than 100 mm/s (green line) are therefore not feasible for seismic observation regardless of instrument, since at these velocities particles would at least temporarily lose contact with the surface. On the other hand, the LDV sensitivity depends primarily on the laser coherence, which constrains the minimum observable Doppler shift, controlled by the laser characteristics. For example, a laser line width around 0.1 kHz (red line), corresponds to less than 0.1 mm/s ground velocity. We conclude that a broad combination of frequencies and displacements can be sampled on small planetary bodies using remote orbital LDVs.

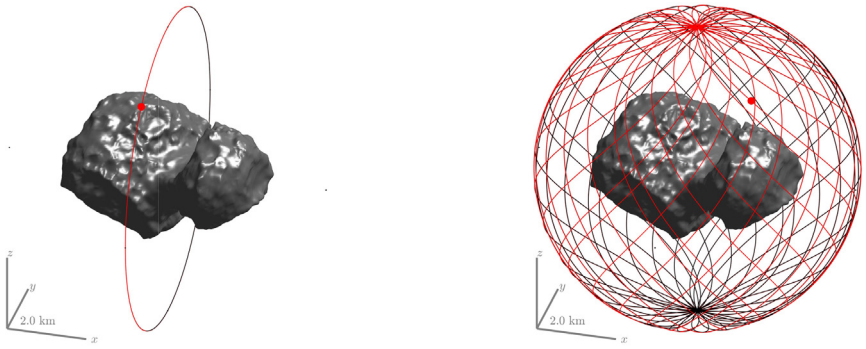
6. Orbital seismic acquisition

Many seismic data acquisition configuration are possible, given the intrinsic mobility of orbital LDV systems. As discussed in the preceding sections, for vector ground velocity acquisition we need to consider multiple (e.g. three) coordinated spacecraft, each carrying their own LDV system, but investigating the same point on the surface at a given time.

We investigate orbital seismic acquisition in the vicinity of small bodies assumed to be spinning at a rapid rate around an axis that defines their polar directions. The acquisition is done from spacecraft moving slowly in polar orbits, in a similar concept of data acquisition as a global radar investigation (Safaeinili et al., 2002), Fig. 9(a). In a reference frame defined relative to the small body, the spacecraft follow helical trajectories, thus allowing the LDV systems to sample multiple locations around the body as a function of time, Fig. 9(b). The density of vantage points from the spacecraft depends on the acquisition duration and on the rotation period of the body. For appropriately chosen orbiter periods that do not match the small body rotation period, the trajectories around the small body do not repeat, and therefore sampling density progressively increases towards a full sphere.

Vector reconstruction of ground velocity requires three spacecraft simultaneously orbiting above a small body. In practice, a triplet of spacecraft is difficult to fly in this kind of formation around a small body, given the irregular gravity field and the influence of solar radiation pressure. However, for well-designed orbits one can optimize the number of three-spacecraft looks. Flying more spacecraft would significantly improve the number of triple simultaneous observations. If the investigation goal is to observe just the propagation times between various points on opposite sides of the small body, then we could use a simpler system with a single spacecraft in orbit around the small body. For this study we assume spacecraft to be flown in differently-inclined polar orbits, with similar orbital radii Fig. 10(b)–(d).

The period of a spacecraft in orbit around a small body is on the order of hours, much longer than the seismic crossing time which is on the order of seconds. Thus, the LDV triplets hover above a region of the small body for a relative long time. The long hover time makes it possible to orient the LDV systems toward different points on the



(a) (b)

Fig. 9. Trajectory of a spacecraft in polar orbit represented (a) in space-fixed coordinates and (b) in body-fixed coordinates. Relative to the body, the LDV orbiter follows a helical trajectory providing the LDV system with vantage points that progressively cover the entire small body surface.

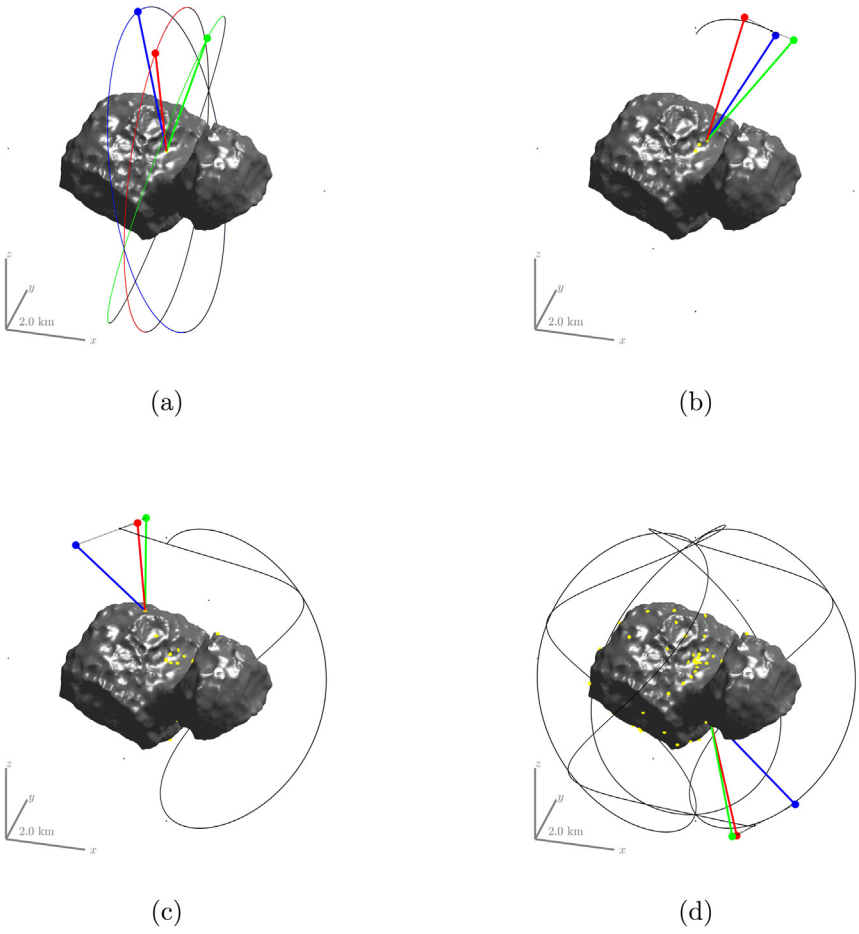


Fig. 10. (a) Orbital acquisition of ground velocity using three coordinated spacecraft in (tilted) polar orbits. (b)–(d) Configuration of the LDV system as a function of acquisition time; the graph shows in yellow all ground points sampled previously. The spacecraft and the associated laser beams are color-coded red/green/blue. (For interpretation of the references to colour in this figure legend, the reader is referred to the web version of this article.)

ground, and therefore achieve higher coverage than what the orbit projection on the surface would otherwise suggest, Fig. 11.

7. Seismic wavefield imaging

Asteroids and comets have highly irregular shapes, Fig. 1. Their internal structure might be comparably irregular, although this is not yet known. We advocate for the use of wavefield imaging methods which can exploit the entire recorded waveforms and can thus lead to high-quality images in complex geology. Wavefield imaging techniques are most developed in the context of exploration seismology and can be adapted to image the interior of the Earth at all scales, from global (Dahlen and Tromp, 1998; Nolet, 2008), to crustal (Berkhout, 1982; Clærbout, 1985; Sherriff and Geldart, 2010, Yilmaz, 2001), to near-surface (Everett, 2013).

Several special features differentiate seismology on a small body from its large body counterpart:

1. We can reliably assume that the exterior shape of the studied object is known with high accuracy, certainly at much higher resolution than the seismic wavelength estimated to be in the order of tens to hundreds of meters. Such information can be obtained from photogrammetry, as is routinely done for planetary objects of all sizes and shapes (Preusker et al., 2015).
2. Seismic waves propagating inside a small body are confined to its interior, since they cannot escape into vacuum due to the lack of elastic support. Thus, seismic energy reverberates for a long time, possibly tens of minutes or more (Walker et al., 2006), and traverse the object repeatedly and in many different directions, while reflecting on the known exterior boundary.
3. The small body interior can be observed from all directions, thus providing subsurface illumination comparable to that provided by a medical tomograph. In contrast, terrestrial seismology uses data acquired on only one side of the imaged volume, thus degrading image accuracy and resolution.

These features significantly aid interior imaging of small bodies, because the known exterior boundary coupled with long propagation times provide a diverse collection of paths inside the object. Moreover, imaging in the presence of known and strong reflectors, i.e. the shape boundary, provides rear-view mirrors that can further constrain

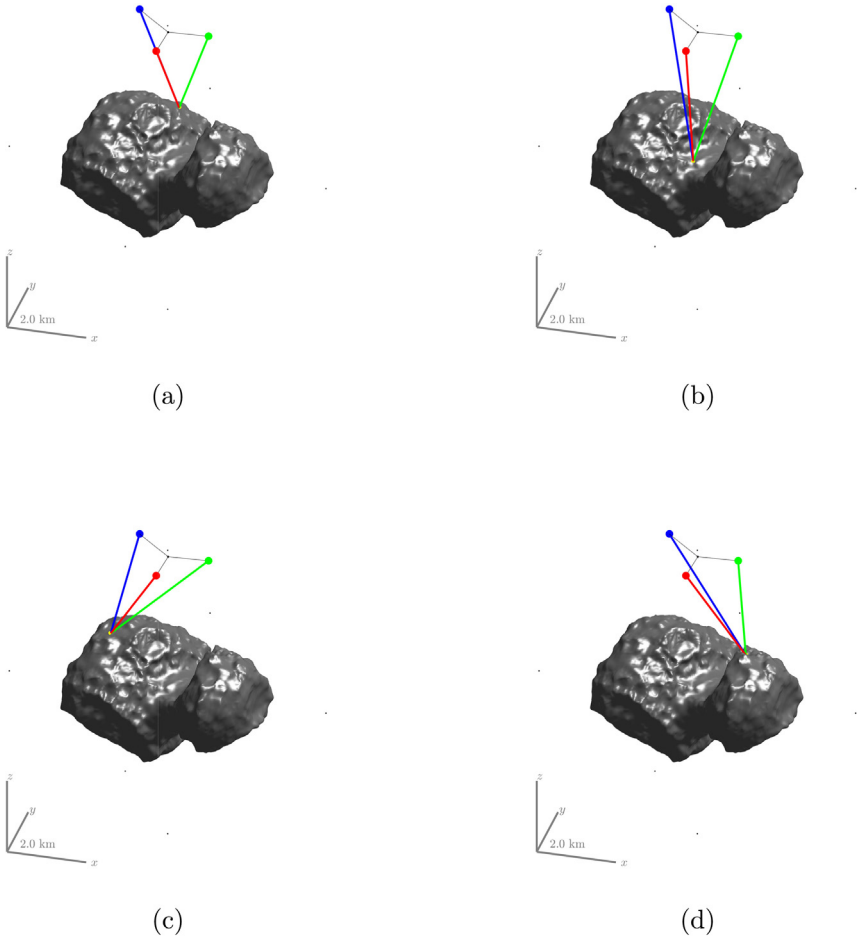


Fig. 11. The ground velocity could be observed at multiple points from any particular configuration of the coordinated orbital LDVs.

physical properties in the body interior (Sava and Asphaug, 2018a,b). In this context, a highly irregular object is actually beneficial for imaging, since multiple reflections on its boundary traverse the body on many diverse paths. The wave-path diversity increases interior imaging resolution, analogously to how multiple views in a medical tomograph form high resolution images.

Wavefield imaging produces a representation of physical properties of the studied object, and can be separated conceptually in two main categories. The first is *tomography*, a technique designed to infer volumetric properties, e.g. the seismic velocity, at every location in the small body interior. The second is *migration*, a technique designed to infer interface properties, e.g. the regions of high contrast between different physical properties. The two classes of techniques work in tandem, such that information providing by one aids and improves the accuracy of the other. In this paper, we emphasize the wavefield imaging technique known as *reverse time migration* (Baysal et al., 1983; McMechan, 1983; Lailly, 1983). This imaging method represents the state-of-the-art in crustal and exploration seismology, and it exploits known principles of time-reversal (Fink et al., 2002).

Reverse time migration is a linear process based on a modeling (or de-migration) operator $\mathbf{M}$ relating the observed data $\mathbf{d}$ with the interior elastic image $\mathbf{i}$:

$$\mathbf{d} = \mathbf{M}\mathbf{i}. \tag{26}$$

Migration forms an image by the application of the adjoint operator $\mathbf{M}^\top$ to the recorded data:

$$\mathbf{i}_{RTM} = \mathbf{M}^\top \mathbf{d}. \tag{27}$$

In practice, migration is executed by back-propagating data from their observation point to all interior locations, followed by the application of an imaging condition which identifies the locations of interior scatterers from properties of the wavefield (e.g. focusing or time coincidence), (Sava and Asphaug, 2018a).

The resolution of reverse-time migration on a small body is in principle limited by the seismic bandwidth. However, a complementary technique known as *least-squares migration* (Chavent and Plessix, 1999; Nemeth et al., 1999; Aoki and Schuster, 2009; Dai et al., 2012; Sava and Asphaug, 2018a) further increases the image resolution by deconvolving the imaging point spread function. Least-squares migration minimizes the objective function

$$\min_{\mathbf{i}} 2J(\mathbf{i}) = \|\mathbf{d} - \mathbf{M}\,\mathbf{i}\|^2 \tag{28}$$

with respect to the image $\mathbf{i}$. Minimizing the objective function from Eq. (28) optimally relates through the demigration operator $\mathbf{M}$ the recorded data $\mathbf{d}$ and the reflectivity image $\mathbf{i}$ (Tarantola, 1987; Aster et al., 2005):

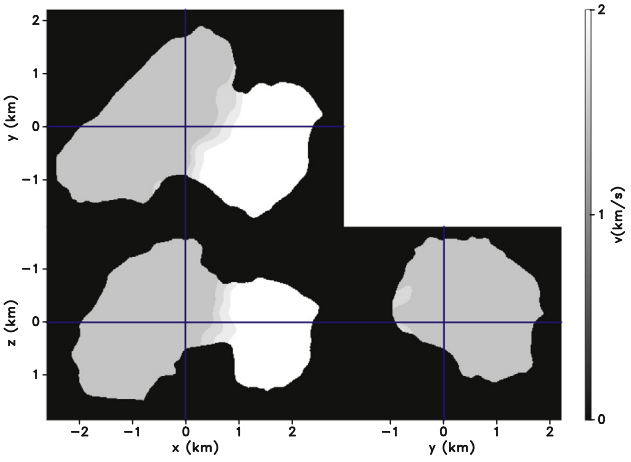


Fig. 12. Velocity model based on the shape of comet 67P/C-G. The model hypothesizes that the two lobes of the comet have different elastic properties, separated by a fracture zone which is subject to repeated seismic activity.

$$\mathbf{i}_{LSM} = \left(\mathbf{M}^{\top}\mathbf{M}\right)^{-1}\mathbf{M}^{\top}\,\mathbf{d}. \tag{29}$$

Least-squares migration achieves high resolution by deconvolving the point spread function $\mathbf{M}^{\top}\mathbf{M}$ from the reverse time migration image $\mathbf{i}_{RTM} = \mathbf{M}^{\top}\mathbf{d}$.

We illustrate the power of seismic wavefield imaging using orbital LDV acquisition with a model based on the geometry of comet 67P/C-G, Fig. 12. We assume LDV acquisition from a spacecraft in polar orbit, Fig. 9, revolving around the small body for 90 days. Ground sampling density increases progressively with acquisition duration, as seen in Fig. 13.

Our example simulates the case of many internal sources activated repeatedly at variable time intervals, e.g. due to comet activity around perihelion. The seismic sources associated with the repeated outbursts are located around fractures separating the two main lobes of the small body, as seen in Fig. 12. We describe the wavefield behavior under the *exploding reflector model* (Clærbout, 1985), which conveniently characterizes wave propagation from sources in the interior of the model to the LDV receivers on the surface. The exploding reflector model has the benefit that all acquired data are processed as a single experiment, instead of a collection of separate experiments. This concept, therefore, reduces the imaging computational cost since only one migration is needed for all data. The simulated wavefields assume a wideband Ricker wavelet of 15 Hz

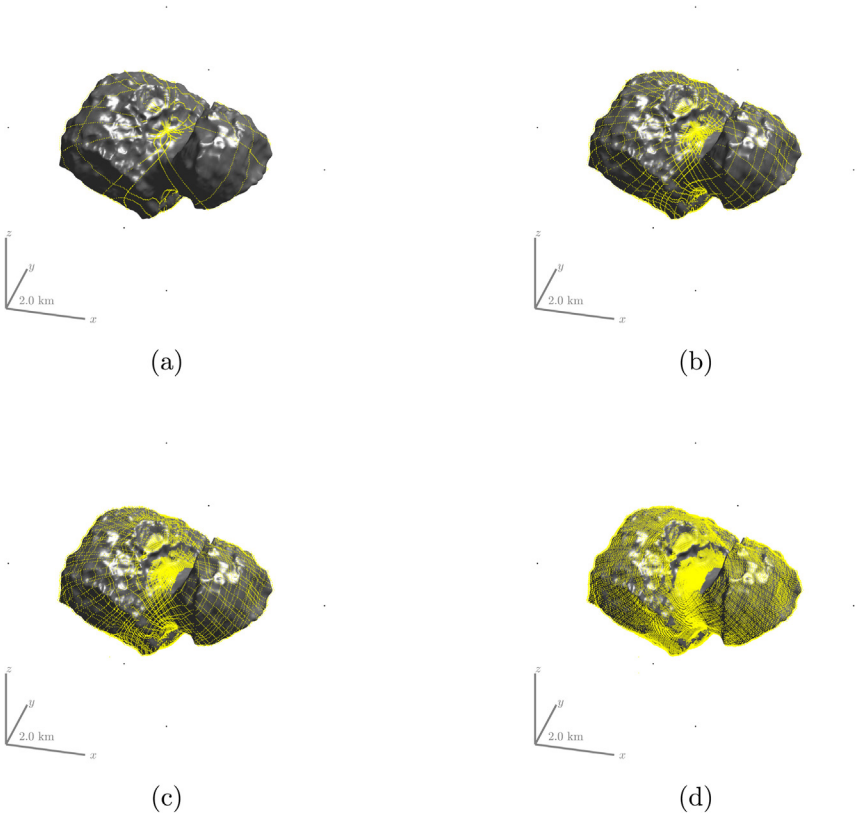


Fig. 13. Collection of ground sampling points for LDVs in polar orbit as shown in Fig. 9. The yellow dots correspond to (a) 5, (b) 15, (c) 30 and (d) 90 days of acquisition, respectively. (For interpretation of the references to colour in this figure legend, the reader is referred to the web version of this article.)

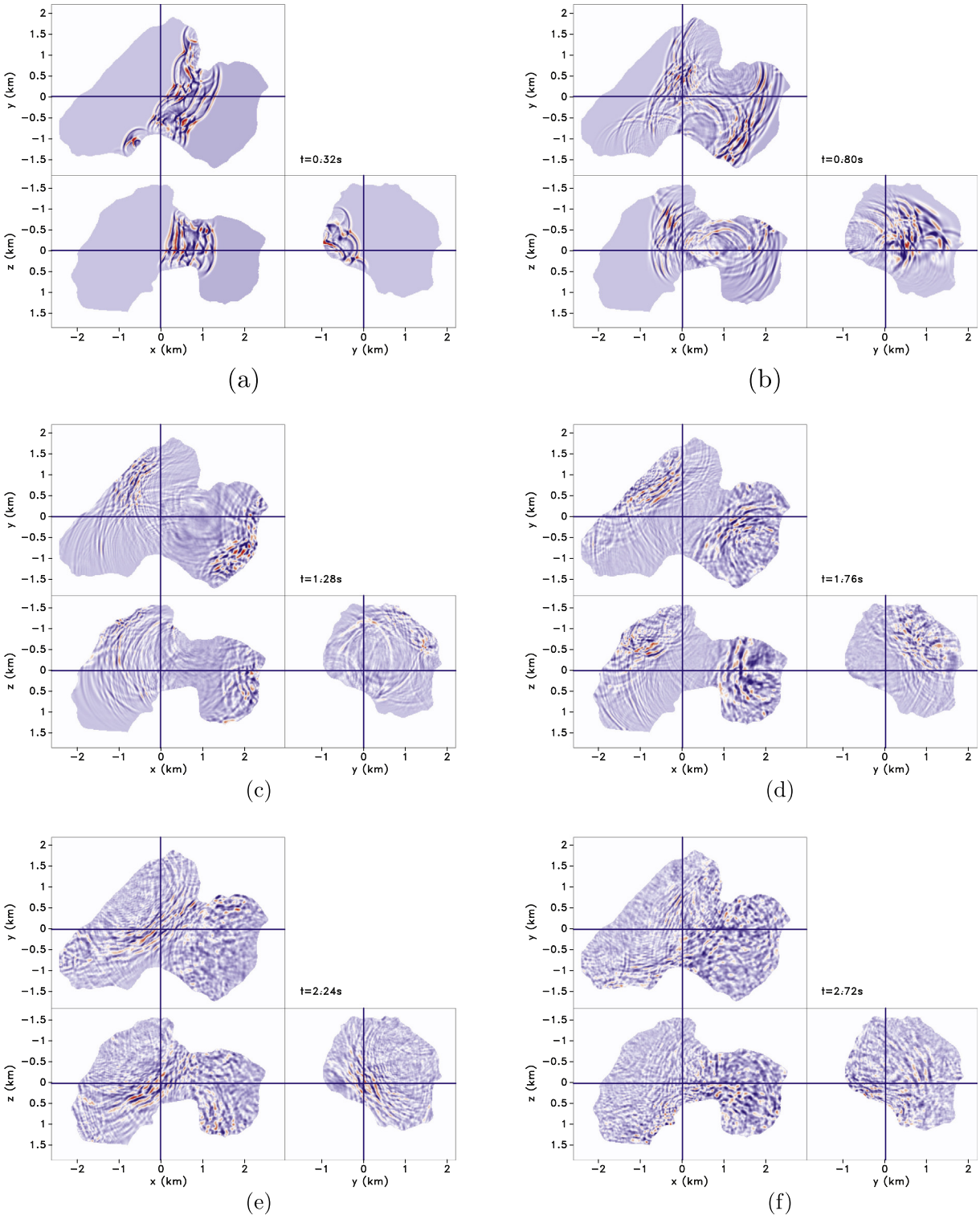


Fig. 14. Seismic wavefields at successive times (labeled on each panel) showing increasing wavefield complexity due to repeated reflections in the interior of the small body.

peak frequency, Fig. 14. The seismic waves interact repeatedly with the small body, and the wavefields rapidly become complex and ultimately chaotic after long interaction with the internal structure and the complex exterior shape reflector. Such data, as seen in Fig. 17, are impossible to interpret without 3D imaging that accurately accounts for wave propagation in the body interior and for the irregular LDV surface acquisition.

Least-squares reverse-time migration focuses correctly the scattered energy at the scatterer positions, thus

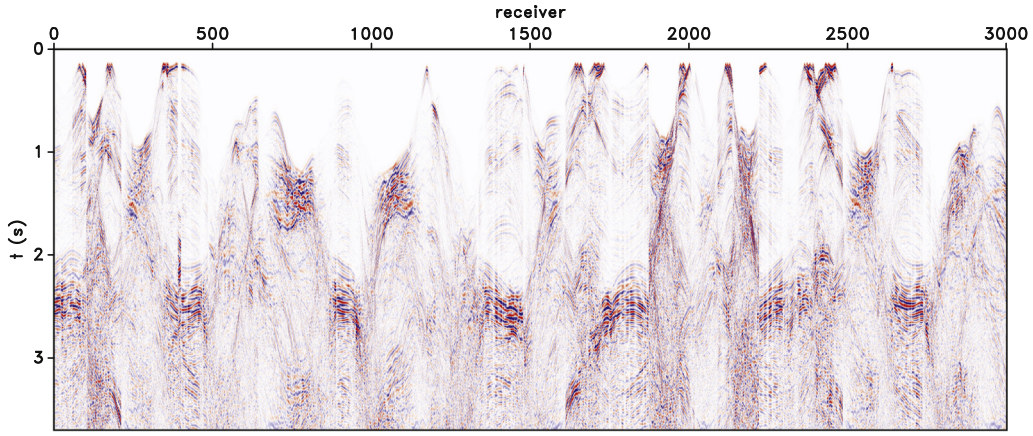


Fig. 15. Seismic wavefields that would be observed at the surface of the small body. The horizontal axis represents the seismic acquisition points distributed irregularly over the small body surface, Fig. 13. The red/blue colors represent positive/negative values of the ground oscillation. Data from a subset of the LDV observation points are shown, for clarity. Data from many other acquisition points are available for imaging, but not shown in this figure. (For interpretation of the references to colour in this figure legend, the reader is referred to the web version of this article.)

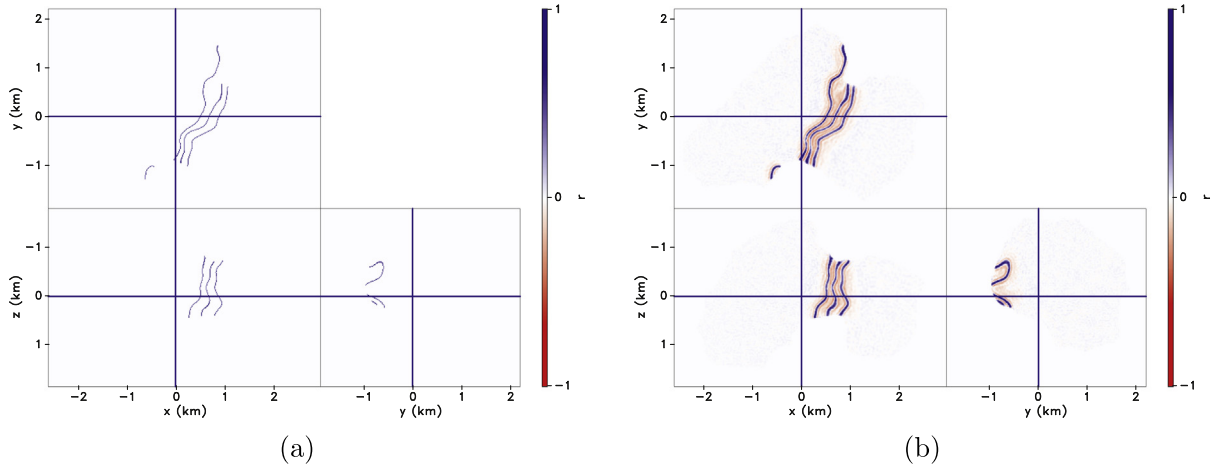


Fig. 16. (a) Ideal geometry of the interior scatterers along the fracture zone, and (b) the image obtained by least-squares reverse time migration.

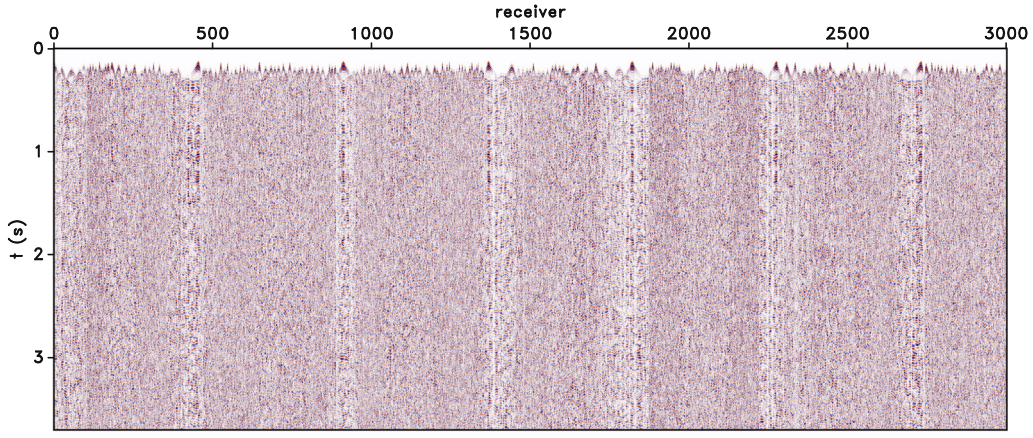


Fig. 17. Seismic wavefields that would be observed at the surface of the small body for a collections of scatterers regularly distributed in the small body interior. This figure follows an identical layout with Fig. 15.

delineating the seismicaly-active fracture zone, Fig. 16. In addition, this technique represents interior reflectivity with sub-wavelength resolution after removal of the point-spread-functions characterizing acquisition and interior illumination. Given the dense acquisition enabled by the LDV system positioned around the small body, the

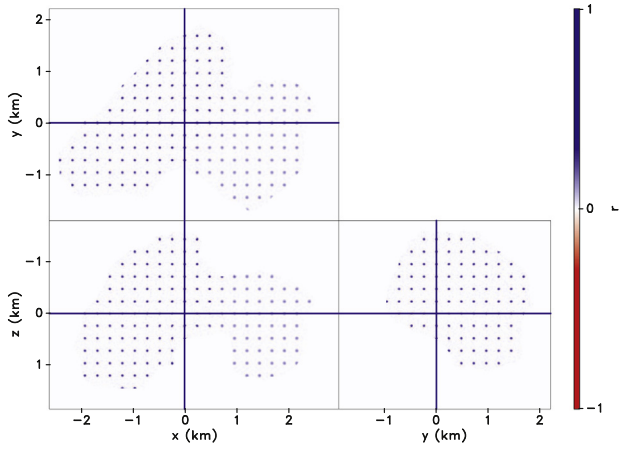


Fig. 18. Least-squares reverse time migration image of the data shown in Fig. 17, indicating good focusing at all locations in the small body interior. The image resolution is sub-wavelength and the same in all directions.

image resolution is high at all interior locations. Fig. 18 demonstrates this feature with an image of scatterers regularly distributed throughout the interior of the body. All scatterers are imaged equally well, and their resolution is identical in all directions, given the dense 3D acquisition achieved with the mobile orbital LDV system. The simulated data for this scenario look effectively random, Fig. 17, and could not be interpreted without 3D imaging, as discussed before.

8. Conclusions

Landing on an asteroid, comet, or small moon is a difficult challenge, especially if the goals are to ensure ground coupling and to transmit large quantities of seismic data to an orbiting spacecraft. Remote sensing from orbit, on the other hand, is becoming a familiar path to cost-effective science missions. Here we present the first study of remote-sensing seismology, opening up the possibility of imaging at high-resolution the mechanical interior of a target small body. A suitably larger optical system could enable long duration and repeated seismic monitoring of planetary surfaces, for instance the Moon and Mars, from a planetary orbiter.

Laser Doppler vibrometer (LDV) systems are effective for recording the (vector) ground motion at the surface of a small body, and are superior to conventional acquisition using seismometers for several reasons: (1) sense ground motion from orbit, without landing; (2) do not require ground coupling and anchoring; (3) do not have sensitive mechanical components; (4) are mobile and can provide global coverage; (5) operate from stable and robust orbital platforms.

The ability to conduct seismology from a remote sensing platform enables a new class of geophysics missions in the solar system that can avoid the complexity and mass of landed payloads, while conducting detailed 3D imaging of internal structure. Seismic data with dense global acquisition would enable the application of state-of-the-art imaging techniques like wavefield migration and tomography. These methods can generate interior images of elastic properties at a resolution comparable to or below the observed seismic wavelength, by exploiting the known complex shape of the small body under investigation.

Acknowledgments

This work was supported by the NASA Planetary Instrument Concepts for the Advancement of Solar System Observations (PICASSO) program (NNH16ZDA001N). The Center for Wave Phenomena at Colorado School of Mines provided logistic and computational support. The reproducible numeric examples used the Madagascar open-source software package (Fomel et al., 2013), freely available from www.ahay.org.

Appendix A. Doppler frequency shift

Consider a laser Doppler vibrometer separated from the ground by an arbitrary distance. The ground is moving relative to the LDV at speed v in the direction of the laser beam. We can describe the relative motion between the LDV and the ground either in a coordinate system referenced to the LDV, or in a coordinate system referenced to the ground, Fig. A.19.

- In the coordinate system referenced to the ground, an electromagnetic wave of frequency f_i propagating from the LDV is observed with the apparent frequency f_g which is related to f_i by

$$f_g = f_i + \frac{v}{\lambda_i}, \tag{A.1}$$

where the wavelength λ_i depends on the frequency f_i as

$$\lambda_i = \frac{c}{f_i} \tag{A.2}$$

and c is the speed of light. By substitution, we obtain

$$f_g = f_i + f_i \frac{v}{c} = f_i\left(1 + \frac{v}{c}\right). \tag{A.3}$$

- In the coordinate system referenced to the LDV, an electromagnetic wave of frequency f_g propagating from the ground is observed at the light detector with the apparent frequency f_r which is related to f_g by

$$f_r = f_g + \frac{v}{\lambda_g}, \tag{A.4}$$

where the wavelength λ_g depends on the frequency f_g as

$$\lambda_g = \frac{c}{f_g}. \tag{A.5}$$

By substitution, we obtain

$$f_r = f_g + f_g \frac{v}{c} = f_g\left(1 + \frac{v}{c}\right). \tag{A.6}$$

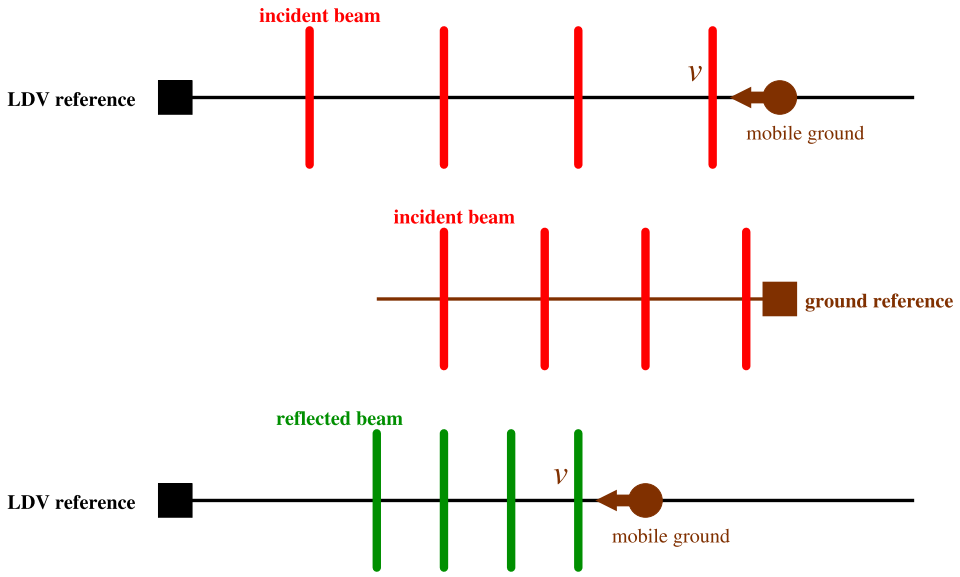


Fig. A.19. Illustration of the Doppler effect. The red and green lines correspond to the incident and reflected beams, respectively. The horizontal distance between consecutive red or green vertical lines indicates the laser beam wavelength. Boxes indicate fixed objects, and circles indicate moving objects. (For interpretation of the references to colour in this figure legend, the reader is referred to the web version of this article.)

Eliminating f_g from Eqs. (A.3) and (A.6) gives:

$$f_r = f_i\left(1+\frac{v}{c}\right)^2 \tag{A.7}$$

Using the fact that the ground velocity $v \ll c$, we can approximate

$$f_r \approx f_i\left(1+2\frac{v}{c}\right). \tag{A.8}$$

The difference between frequency f_r of the reflected beam and the frequency f_i of the incident beam

$$\Delta f \equiv f_r - f_i = 2f_i\frac{v}{c} = \frac{2}{\lambda_i}v \tag{A.9}$$

represents the Doppler shift characterizing an object moving at velocity v in the direction of the laser beam. The Doppler frequency shift is directly proportional to the ground velocity v in the direction of the beam.

References

Aoki, N., Schuster, G., 2009. Fast least-squares migration with a deblurring filter. Geophysics, WCA83–WCA93.

Asphaug, E., 2008. Critical crater diameter and asteroid impact seismology. Meteor. Planet. Sci. 43 (6), 1075–1084.

Asphaug, E., 2009. Growth and evolution of asteroids. Ann. Rev. Earth Planet. Sci. 37 (1), 413–448.

Aster, R., Borchers, B., Thurber, C., 2005. Parameter Estimation and Inverse Problems. Elsevier.

Banerdt, W., Smrekar, S., Longone, P., 2013. InSight: a discovery mission to explore the interior of Mars. In: Lunar and Planetary Science Conference, p. 1915.

Baysal, E., Kosloff, D., Sherwood, J., 1983. Reverse time migration. Geophysics 48 (11), 1514–1524.

Berkhout, A.J., 1982. Imaging of Acoustic Energy by Wave Field Extrapolation. Elsevier.

Binzel, R., Reddy, V., Dunn, T., 2015. The Near-Earth Object Population: Connections to Comets, Main-Belt Asteroids, and Meteorites, Asteroids IV. University of Arizona Press.

Blitz, C., 2009. Ejecta and Wave Propagation Simulation in Asteroids: Application to Crater Erasure on Asteroid 433-Eros. Ph.D. thesis, Institut de Physique du Globe de Paris - IPGP.

Bruck Syal, M., Owen, J.M., Miller, P.L., 2016. Deflection by kinetic impact: sensitivity to asteroid properties. Icarus 269, 50–61.

Chavent, G., Plessix, R., 1999. An optimal true-amplitude least-squares prestack depthmigration operator. Geophysics, 508–515.

Ciarletti, V., Herique, A., Lasue, J., Levasseur-Regourd, A.-C., Plettemeier, D., Florentin, L., Christophe, G., Pierre, P., Kofman, W., 2017. CONSERT constrains the internal structure of 67P at a few-metre size scale. Monthly Notices of the Royal Astronomical Society, 3132.

Clærbout, J.F., 1985. Imaging the Earth's Interior. Blackwell Scientific Publications.

Dahlen, F.A., Tromp, J., 1998. Theoretical Global Seismology. Princeton University Press.

Dai, W., Fowler, P., Schuster, G., 2012. Multi-source least-squares reverse time migration. Geophys. Prospect. 60 (4), 681–695.

Daly, M.G., Barnouin, O.S., Dickinson, C., Seabrook, J., Johnson, C.L., Cunningham, G., Haltigin, T., Gaudreau, D., Brunet, C., Aslam, I., Taylor, A., Bierhaus, E.B., Boynton, W., Nolan, M., Lauretta, D.S., Oct 2017. The OSIRIS-Rex Laser Altimeter (OLA) investigation and instrument. Space Sci. Rev. 212 (1), 899–924.

Donges, A., Noll, R., 2015. Laser Measurement Technology: Fundamentals and Applications. Springer.

Drabenstedt, A., 2007. Quantification of displacement and velocity noise in vibrometer measurements on transversely moving or rotating surfaces. In: Proceedings of SPIE – The International Society for Optical Engineering. p. 6616.

Everett, M., 2013. Near-Surface Applied Geophysics. Cambridge University Press.

Fink, M., Kuperman, W., Montagner, J.-P., 2002. Imaging of Complex Media with Acoustic and Seismic Waves. Springer.

Fomel, S., Sava, P.C., Vlad, I., Liu, Y., Bashkardin, V., 2013. Madagascar: open-source software project for multidimensional data analysis and reproducible computational experiments. J. Open Res. Software 1 (1), e8.

Fujiwara, A., Kawaguchi, J., Yeomans, D.K., Abe, M., Mukai, T., Okada, T., Saito, J., Yano, H., Yoshikawa, M., Scheeres, D.J.,

Barnouin-Jha, Cheng, A.F., Demura, H., Gaskell, R.W., Hirata, N., Ikeda, H., Kominato, T., Miyamoto, H., Nakamura, A.M., Nakamura, R., Sasaki, S., Uesugi, K., 2010. The rubble-pile asteroid Itokawa as observed by Hayabusa. Science 312 (5778), 1330–1334.

Gowen, R., Smith, A., Fortes, A., Barber, S., Brown, P., Church, P., Collinson, G., Coates, A., Collins, G., Crawford, I., Dehant, V., Chela-Flores, J., Griffiths, A., Grindrod, P., Gurvits, L., Hagermann, A., Hussmann, H., Jaumann, R., Jones, A., Joy, K., Karatekin, O., Miljkovic, K., Palomba, E., Pike, W., Prieto-Ballesteros, O., Raulin, F., Sephton, M., Sheridan, S., Sims, M., Storrie-Lombardi, M., Ambrosi, R., Fielding, J., Fraser, G., Gao, Y., Jones, G., Kargl, G., Karl, W., Macagnano, A., Mukherjee, A., Muller, J., Phipps, A., Pullan, D., Richter, L., Sohl, F., Snape, J., Sykes, J., Wells, N., 2011. Penetrators for in situ subsurface investigations of Europa. Adv. Space Res. 48 (4), 725–742.

Guo, G., Li, S., Tan, Q., 2001. Statistical properties of laser speckles generated from far rough surfaces. Int. J. Infrared Millimeter Waves 22, 1177–1191.

Hurford, T.A., Asphaug, E., Spitale, J.N., Hemingway, D., Rhoden, A.R., Henning, W.G., Bills, B.G., Kattenhorn, S.A., Walker, M., 2016. Tidal disruption of Phobos as the cause of surface fractures. J. Geophys. Res.: Planets 121 (6), 1054–1065.

Lailly, P., 1983. The seismic inverse problem as a sequence of before stack migrations. In: Proceedings of the Conference on Inverse Scattering, Theory and Application, pp. 206–220.

Lucey, P.G., Neumann, G.A., Riner, M.A., Mazarico, E., Smith, D.E., Zuber, M.T., Paige, D.A., Bussey, D.B., Cahill, J.T., McGovern, A., Isaacson, P., Corley, L.M., Torrence, M.H., Melosh, H.J., Head, J.W., Song, E., 2014. The global albedo of the Moon at 1064 nm from LOLA. J. Geophys. Res.: Planets 119 (7), 1665–1679.

Massironi, M., Simioni, E., Marzari, F., Cremonese, G., Giacomini, L., Pajola, M., Jorda, L., Naletto, G., Lowry, S., El-Maarry, M.R., Preusker, F., Scholten, F., Sierks, H., Barbieri, C., Lamy, P., Rodrigo, R., Koschny, D., Keller, H.R.H.U., A'Hearn, M.F., Agarwal, J., Auger, A.-T., Barucci, M.A., Bertaux, J.-L., Bertini, I., Besse, S., Bodewits, D., Capanna, C., Deppo, V.D., Davidsson, B., Debei, S., Cecco, M.D., Ferri, F., Fornasier, S., Fulle, M., Gaskell, R., Groussin, O., Gutiérrez, P.J., Güttler, C., Hviid, S.F., Ip, W.-H., Knollenberg, J., Kovacs, G., Kramm, R., Kührt, E., Küppers, M., Forgia, F.L., Lara, L.M., Lazzarin, M., Lin, Z.-Y., Moreno, J.J.L., Magrin, S., Michalik, H., Mottola, S., Oklay, N., Pommerol, A., Thomas, N., Tubiana, C., Vincent, J.-B., 2015. Two independent and primitive envelopes of the bilobate nucleus of comet 67P. Nature 526, 402–405.

McMechan, G., 1983. Migration by extrapolation of time-dependent boundary values. Geophys. Prospect. 31 (3), 413–420.

Miyashita, T., Fujino, Y., 2006. Development of 3D vibration measurement system using Laser Doppler Vibrometers. In: Proceedings of SPIE - The International Society for Optical Engineering. p. 6177.

Morrison, D., Chapman, C.R., Steel, D., Binzel, R.P., 2004. Impacts and the Public: Communicating the Nature of the Impact Hazard. Cambridge University Press, 353–390.

Neal, C., Banerdt, W., Alkalai, L., 2011. LUNETTE: a two-lander Discovery-class geophysics mission to the Moon. In: Lunar and Planetary Science Conference, p. 2832.

Nemeth, T., Wu, C., Schuster, G., 1999. Least-squares migration of incomplete reflection data. Geophysics, 208–221.

Nesvorný, D., Broz, M., Carruba, V., 2015. Identification and Dynamical Properties of Asteroid Families, Asteroids IV. University of Arizona Press.

Nolet, G., 2008. A Breviary of Seismic Tomography: Imaging the Interior of the Earth and Sun. Cambridge University Press.

Preusker, F., Scholten, F., Matz, K.-D., Roatsch, T., Willner, K., Hviid, S.F., Knollenberg, J., Jorda, L., Gutiérrez, P.J., Kührt, E., Mottola, S., A'Hearn, M.F., Thomas, N., Sierks, H., Barbieri, C., Lamy, P., Rodrigo, R., Koschny, D., Rickman, H., Keller, H.U., Agarwal, J., Barucci, M.A., Bertaux, J.-L., Bertini, I., Cremonese, G., Da Deppo, V., Davidsson, B., Debei, S., De Cecco, M., Fornasier, S., Fulle, M., Groussin, O., Güttler, C., Ip, W.-H., Kramm, J.R., Küppers, M., Lara, L.M., Lazzarin, M., Lopez Moreno, J.J., Marzari, F., Michalik, H., Naletto, G., Oklay, N., Tubiana, C., Vincent, J.-B., 2015. Shape model, reference system definition, and cartographic mapping standards for comet 67P/Churyumov-Gerasimenko – stereo-photogrammetric analysis of Rosetta/OSIRIS image data. Astron. Astrophys. 583, A33.

Richardson, J., Melosh, H., Greenberg, R., O'Brien, D., 2005. The global effects of impact-induced seismic activity on fractured asteroid surface morphology. Icarus 179 (2), 325–349.

Rothberg, S., Allen, M., Castellini, P., Maio, D.D., Dirckx, J., Ewins, D., Halkon, B., Muyshondt, P., Paone, N., Ryan, T., Steger, H., Tomasini, E., Vanlanduit, S., Vignola, J., 2017. An international review of Laser Doppler Vibrometry: making light work of vibration measurement. Opt. Lasers Eng. 99, 11–22.

Safaeinili, A., Gulkis, S., Hofstadter, M., Jordan, R., 2002. Probing the interior of asteroids and comets using radio reflection tomography. Meteor. Planet. Sci. 37, 1953–1963.

Sava, P.C., Asphaug, E., 2018a. 3D radar wavefield migration of comet interiors. Adv. Space Res. 62, 1146–1164.

Sava, P.C., Asphaug, E., 2018b. 3D radar wavefield tomography of comet interiors. Adv. Space Res. 61, 2198–2213.

Sava, P.C., Ittharat, D., Grimm, R., Stillman, D., 2015. Radio reflection imaging of asteroid and comet interiors. I: Acquisition and imaging theory. Adv. Space Res. 55, 2149–2165.

Scheeres, D., Chesley, S., Anderson, R., 2014. A Geophysical Laboratory for Rubble Pile Asteroids: The BASiX Mission. AAS/Division for Planetary Sciences Meeting Abstracts vol. 46, 214.16.

Sherriff, R.E., Geldart, L.P., 2010. Exploration Seismology. Cambridge University Press.

Smith, D., Zuber, M., Jackson, G., Cavanaugh, J., Neumann, G., Riris, H., Sun, X., Zellar, R., Coltharp, C., Connelly, J., Katz, R., Kleyner, I., Liiva, P., Matuszeski, A., Mazarico, E., McGarry, J., Novo-Gradac, A., Ott, M., Peters, C., Ramos-Izquierdo, L., Ramsey, L., Rowlands, D., Schmidt, S., Scott, V., Shaw, G., Smith, J., Swinski, J., Torrence, M., Unger, G., Yu, A., Zagwodzki, T., 2010. The Lunar Reconnaissance Orbiter laser ranging investigation. Space Sci. Rev. 150, 209–241.

Smith, D.E., Zuber, M.T., Neumann, G.A., Lemoine, F.G., Mazarico, E., Torrence, M.H., McGarry, J.F., Rowlands, D.D., Head, J.W., Duxbury, T.H., Aharonson, O., Lucey, P.G., Robinson, M.S., Barnouin, O.S., Cavanaugh, J.F., Sun, X., Liiva, P., Mao, D., Smith, J.C., Bartels, A.E., 2010. Initial observations from the Lunar Orbiter Laser Altimeter (LOLA). Geophys. Res. Lett. 37 (18), l18204.

Tanaka, S., Mitani, T., Otake, H., Ogawa, K., Kobayashi, N., Hashimoto, T., Hoshino, T., Otsuki, M., Wakabayashi, S., Kimura, J., Kuramoto, K., 2013. Present status of the Lunar lander project SELENE-2. In: Lunar and Planetary Science Conference. p. 1838.

Tarantola, A., 1987. Inverse Problem Theory: Methods for Data Fitting and Model Parameter Estimation. Elsevier.

Thomas, P., Robinson, M., 2005. Seismic resurfacing by a single impact on the asteroid 433 Eros. Nature 436, 366–369.

Tong, V., Garcia, R., 2015. Extraterrestrial Seismology. Cambridge University Press.

Voirin, T., Larranaga, J., Taylor, G., Sanchez Perez, J., Cavel, J.P.C., Falkner, P., 2014. Inspire: a Mars network science mission. In: 11th International Planetary Probe Workshop, p. 8040.

Walker, J., Sagebiel, E., Huebner, W., 2006. A preliminary analysis of seismological techniques to study Eros and other asteroids. Adv. Space Res. 37, 142–152.

Yilmaz, O., 2001. Seismic Data Analysis, second ed. Society of Exploration Geophysicists.

Zuber, M., Smith, D., Zellar, R., Neumann, G., Sun, X., Katz, R., Kleyner, I., Matuszeski, A., McGarry, J., Ott, M., Ramos-Izquierdo, L., Rowlands, D., Torrence, M., Zagwodzki, T., 2010. The lunar reconnaissance orbiter laser ranging investigation. Space Sci. Rev. 150, 63–80.